Research On Weld Defects Detection Method Based On Laser Ultrasound And CBAM-CNN

Bo-Yu Ning[1], Shang-Fei Zheng[1], Cui Sen[1], Gui-Dong Xu[1], Chen-Guang Xu[1], and Sai Zhang[1*]

[1] School of Physics and Electronic Engineering, Jiangsu University, Zhenjiang 212013, China
[*] Corresponding author. E-mail: zhangsai@ujs.edu.cn

Received: Mar. 03, 2025; Accepted: Aug. 03, 2025

A novel weld defect detection methodology by integrating laser ultrasonic technology with a convolutional neural network (CNN) enhanced through a convolutional block attention module (CBAM), aiming to improve the accuracy and efficiency of defect characterization in industrial non-destructive testing. The approach begins with the establishment of a finite element model using COMSOL Multiphysics to simulate laser-ultrasound interactions with distinct weld defect . The acquired one-dimensional time-domain signals are then transformed into two-dimensional time-frequency representations using continuous wavelet transform (CWT), optimizing the data for deep learning processing. A CBAM-CNN architecture is subsequently developed, leveraging channel-spatial attention mechanisms to enhance feature extraction and suppress noise interference. Experimental results demonstrate exceptional performance, with the model achieving 99.06% mean classification accuracy on pristine test data and maintaining 89.18% accuracy under different Gaussian noise conditions. The model's robustness is further validated through t-SNE visualizations and confusion matrix analyses, confirming its ability to accurately classify porosity defects across varying sizes and noise levels. These findings highlight the method's potential for automated quality inspection in manufacturing, particularly for high-precision weld defect detection.

Keywords: Laser ultrasonic; Convolutional neural network; Defect classification detection; Convolutional block attention module

http://dx.doi.org/10.6180/jase.202605_29(5).0006

1. Introduction

Welding is a key technology widely applied in manufacturing and construction industries, its quality directly affects the structural integrity and safety of the final products. With the development of industrial automation and intelligent manufacturing, higher requirements have been imposed on the detection of weld seam quality [1, 2]. Laser ultrasonic is a non-contact and non-destructive testing technology that features wide frequency band, high spatial resolution and high precision. By detecting the information such as the reflection and transmission of sound waves on the surface of the object, it can identify the internal defects of the object without damaging it [3]. Many studies have been conducted on laser ultrasound non-destructive testing. Kou et al.[4] used laser ultrasound and Synthetic Aperture Focusing Technique (SAFT) to perform fully non-contact non-destructive testing and imaging of internal defects in thick metals. Davis et al. [5] use laser ultrasonic testing (LUT) for inspecting defects in additively manufactured components, demonstrating its potential as a non-contact and effective method. Okuyama et al. [6] summarized the method of detecting porosity in galvanized steel lap welds using laser ultrasound and analyzed the reasons for changes in detection metric values, as well as the relationship between spatial resolution and detection probability. Nothdurft et al. [7] investigates the effects of laser

beam position and ultrasound excitation on the microstructure and weldability of dissimilar low-alloyed steel joints, demonstrating that ultrasound-assisted laser welding can reduce crack formation. Lei et al. [8] proposed a method for detecting the quality of laser spot welds using laser ultrasound and distinguished between standard and false welding by comparing the propagation characteristics of ultrasonic waves in different samples. These studies mainly analyze the signals generated by the interaction between laser-excited ultrasound and defects, relying heavily on human judgment, which may sometimes lead to inaccurate detection results. With the rapid development of deep learning technology and its successful application in image processing, new ideas have emerged for ultrasonic defect detection.

Alqahtani H et al. [9] applied CNN to the collaborative combination of ultrasonic measurements and confocal microscopy images to detect and assess the risk of fatigue damage, demonstrating that both ultrasonic data and images can classify fatigue damage with high accuracy. Park et al. [10] used machinable samples with different porosities and surface roughness to obtain time-domain ultrasonic signals, trained CNN models, and verified that all models can accurately evaluate porosity. Munir et al. [11] applied CNN to noisy ultrasonic signals to improve the classification performance and applicability of weld defects, showing that CNN can achieve high defect classification accuracy even with noisy signals. Jin et al. [12] proposed an intelligent recognition method for concrete ultrasonic testing based on wavelet packet transform and CNN, using K-fold cross-validation for performance analysis and classification experiments, achieving high accuracy. Zhu et al. [13] built an intelligent recognition model based on object detection and tracking algorithms in deep learning, fusing features from S-scan and B-scan images of ultrasonic phased array testing of welds and combining three-dimensional structural information of welds to identify and locate defects in three-dimensional space.

This paper will establish a numerical simulation model of the interaction between laser ultrasound and different weld defects to obtain the required time-domain ultrasonic signals. These signals will then be transformed into two-dimensional time-frequency images using CWT and input into a CNN model combined with CBAM for automatic defect classification and recognition. This method can achieve automatic quantification of defects, avoiding the instability that may arise from manual feature extraction.

2. Materials and methods

2.1. Laser ultrasonic excitation mechanism

When a pulsed laser irradiates the surface of a solid material, a portion of its energy is rapidly absorbed by the surface. Due to the insufficient time for heat diffusion, a transient temperature field with a non-uniform distribution is formed in the near-surface layer around the laser source. The gradient distribution of the temperature field induces localized thermal expansion in the surface layer, thereby generating a stress field. This thermal stress serves as the wavefield source for ultrasonic waves. The resulting stress propagates through the material in the form of a transient pulse, ultimately forming ultrasonic waves. When laser radiation interacts with metallic surfaces, it exhibits a Gaussian distribution characteristic [14]. For two-dimensional modeling, the absorbed pulsed laser energy in the material can be expressed as Eq. (1).

$$-k\frac{\partial T(x,y,t)}{\partial y}\bigg|_{y=h} = I_0 A(t) f(x) g(t) \tag{1}$$

where k represents the thermal diffusivity of the material, $T(x,y,t)$ denotes the time-dependent temperature distribution within the material, I_0 indicates the peak power density of the incident pulsed laser, h corresponds to the sample height, and $A(t)$ signifies the reflectivity coefficient at the metal surface. For the purposes of this study, it is assumed that the entire energy of the pulsed laser is absorbed by the surface layer of the metallic material [15]. $f(x)$ and $g(t)$ denote the spatial and temporal profiles of the laser pulse, which can be expressed as Eq. (2) and Eq. (3),respectively.

$$f(x) = \exp\left(-x^2/R^2\right) \tag{2}$$

$$g(t) = (t/t_0)\,\square\,(-t/t_0) \tag{3}$$

where x represents the radial distance from the center of the laser spot, R denotes the radius of the laser spot, and t_0 corresponds to the pulse rise time.

2.2. Convolutional Block Attention Module

The CBAM is an attention mechanism module designed for convolutional neural networks, primarily composed of a Channel Attention Module (CAM) and a Spatial Attention Module (SAM) [16]. The overall architecture is illustrated in Fig. 1(a). The input feature is represented as $F \in R^{C\times H\times W}$, which denotes a three-dimensional real-valued tensor of the feature map with C channels, a height of H , and a width of W. The computational formula is expressed as Eq. (6) and Eq. (7).

$$F' = M_C(F) \otimes F \tag{6}$$

$$F'' = M_S\left(F'\right) \otimes F' \tag{7}$$

where $M_C \in R^{C\times1\times1}$ denotes one-dimensional feature extraction performed along the channel dimension, while $M_S \in R^{1\times H\times W}$ represents two-dimensional feature extraction conducted in the spatial domain. The output F' is obtained by multiplying the result of the channel attention convolution with the input feature map F. Subsequently, F' is utilized as the input for the spatial attention module, where a two-dimensional convolution is applied, and the result is multiplied with the original feature map to yield the final output F''. The structural diagrams of the channel attention module and the spatial attention module are depicted in Fig. 1(b) and Fig. 1(c), respectively.

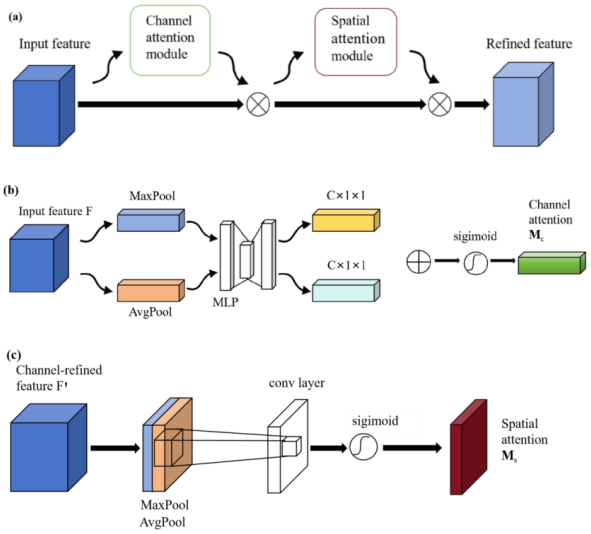

Fig. 1. Structure of (a) convolutional block attention module, (b) channel attention module and (c) spatial attention module

The channel attention module compresses the spatial dimensions while preserving the channel dimensionality.The input feature map, after passing through parallel max-pooling layers and average-pooling layers, is transformed from its original dimensions of C × H × W into two feature maps of dimensions C × 1 × 1. These feature maps are then fed into a multi-layer perceptron (MLP), which first reduces and subsequently expands the number of channels back to the original count. The outputs are summed and passed through a sigmoid activation function to yield the final M_C. The formula is expressed as Eq. (8).

$$M_C(F) = \sigma(MLP(\text{AvgPool}(F)) + MLP(\text{MaxPool}(F))) \tag{8}$$

where σ represents the sigmoid activation function. The spatial attention module performs channel dimension compression while maintaining the spatial dimension unchanged. The output of the CAM is processed through both max pooling and average pooling to generate two feature maps of size 1 × H × W. These two feature maps are then concatenated and passed through a 7 × 7 convolution to produce a single-channel feature map. Subsequently, this feature map is activated by a sigmoid function to obtain the spatial attention feature map. The formula is expressed as Eq. (9).

$$M_S(F) = \sigma\left(f^{7\times7}([\text{AvgPool}(F);\text{MaxPool}(F)])\right) \tag{9}$$

where $f^{7\times7}$ represents the convolution operation utilizing a 7 × 7 convolution kernel.

2.3. Loss function

This study addresses weld defect detection as a multi-class classification task. To effectively distinguish defects of varying sizes, the cross-entropy loss function is adopted.The formula is expressed as Eq. (10).

$$L_{CE} = -\sum_{i=1}^{C} y_i \log\left(Y_i\right) \tag{10}$$

Where C denotes the total number of classes, y_i is the one-hot encoded ground truth label, and Y_i represents the predicted class probability output by the model.The cross-entropy loss function and Softmax function are jointly employed in classification tasks, collectively constituting the output layer and loss computation module of the classification model.

2.4. Modeling and Simulation

Laser ultrasonic serves as an effective method for detecting metal defects. In this study, a two-dimensional welded steel plate model was established using the COMSOL Multiphysics. The model material is isotropic structural steel with material parameters as listed in Table 1. The defect model constructed is illustrated in Fig. 2.The model is composed of two steel plates and the weld area in the middle. The respective areas they belong to are shown by the black solid lines in the figure. The model has a total length of 35 mm , with each of the two steel plates measuring 15 mm in length and 5 mm in height. The weld zone is 5 mm in length and 6 mm in height. The radius of the pore defect is 0.3 mm . The expression for the pulsed laser is as described

above, with the laser excitation center located 3 mm from the left boundary of the model, and the signal reception point positioned 3 mm to the right of the laser center.

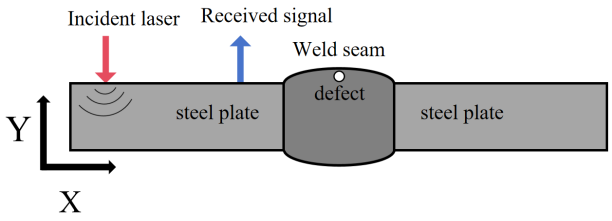

Fig. 2. Two-dimensional model diagram of welded steel plate

When a pulsed laser irradiates the surface of a steel body, the laser energy is absorbed by the metallic material, inducing thermal expansion and consequently generating thermal stress, which excites ultrasonic waves. Therefore, this study employs the physical field coupling of two modules: solid heat transfer and solid mechanics, with the multiphysics module being thermal expansion [17]. To mitigate the influence of boundary reflections on the detection area, the left, right, and bottom boundaries in the solid mechanics module are set as low-reflectivity boundaries, while the remaining boundaries are set as free boundaries. In the solid heat transfer module, the model boundaries are configured as adiabatic, with an initial temperature of 293.15 K. Fig. 3 presents the ultrasonic displacement contour maps of the model containing a pore defect at different time instances. From Fig. 3(a), it can be observed that when the pulsed laser irradiates the metal surface, shear waves (S-waves), longitudinal waves (L-waves), and surface waves (R-waves) are generated [18]. Among these, the surface waves (R-waves) exhibit the highest energy and demonstrate more pronounced interactions with the defect. In Fig. 3(b), the surface waves reflect at the interface between the steel structure and the weld, generating a primary reflected surface wave (RR_1). Subsequently, as shown in Fig. 3(c), the surface waves continue to propagate and interact with the pore defect, resulting in the secondary reflected surface wave (RR_2) and the transmitted wave (TR) depicted in Fig. 3(d).

Fig. 4 illustrates the time-domain signals generated by the interaction of acoustic waves with pore defects of varying radii. When surface waves interact with pore defects of different radii, their propagation characteristics undergo changes and leads to a change in the amplitude of the reflected echo.

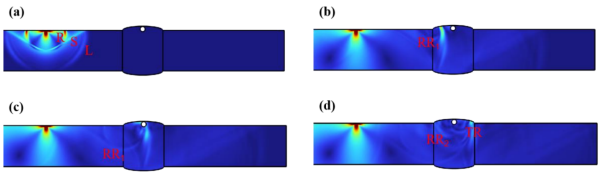

Fig. 3. Displacement cloud diagrams at different times. (a)0.86μs; (b)3.87μs; (c)4.45μs; (d)5.09μs;

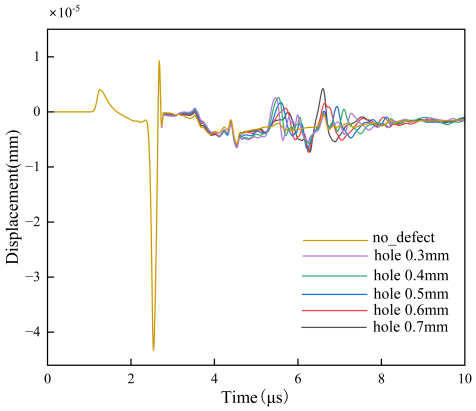

Fig. 4. Time domain signal diagram of defects with different radii

2.5. Signal Processing

In order to transform the acquired one-dimensional time-domain signal data into a two-dimensional time-frequency representation, the CWT is employed to convolve the signal with scaled and shifted wavelet functions, thereby obtaining the representation of the signal at various scales and positions [19]. This method provides localized information on both time and frequency variations and is highly effective in processing non-stationary signals. Therefore, this study employs CWT for signal processing, with its formula given as Eq. (10).

$$W(a,b) = \frac{1}{\sqrt{a}} \int x(t) \psi^* \left(\frac{t-b}{a} \right) dt \tag{11}$$

Where $W(a,b)$ represents the wavelet coefficients, a denotes the scale parameter, b signifies the translation parameter, $\psi^*(t)$ is the complex conjugate form of the wavelet basis function, and $x(t)$ corresponds to the original signal.

When processing laser ultrasonic signals, selecting an appropriate wavelet basis function is crucial for obtaining satisfactory analytical results. There are numerous

Table 1. Material Parameters

	Density $\rho\,(\mathrm{kg/m^3})$	Poisson's Ratio v	Young's Modulus $E(\mathrm{GPa})$	Thermal Expansion Coefficient $\alpha\,(\mathrm{K^{-1}})$
Steel	7800	0.33	210	12.3×10^{-6}
Weld	7800	0.33	192	12.3×10^{-6}

commonly used wavelet basis functions, such as the Morlet wavelet, Mexican Hat wavelet, Haar wavelet, and Daubechies wavelet, among others. The Morlet wavelet, being a complex wavelet, exhibits a geometric shape more akin to that of ultrasonic echo waveforms and offers excellent frequency and time resolution. Consequently, this study opts for the Morlet wavelet. As illustrated in Fig. 5, the two-dimensional time-frequency images are obtained by applying the CWT to the original time-domain signals received from various defects [20]. By controlling the probe to perform parameterized scanning within a range of 4.5–10 mm from the laser excitation source, 55 sets of raw signal data were collected for each type of defect. The collected raw signals were further augmented through left and right rotations of 30°, 60°, 90°, and 120° to enhance the generalization capability of the model during training. A total of 2970 sample images across 6 defect categories were generated, uniformly resized to 300 × 300 pixels, and then partitioned into training, validation, and test sets in a 7:2:1 ratio to meet the requirements of the neural network.

To subsequently validate the generalization capability of the model, Gaussian white noise with signal-to-noise ratios (SNR) ranging from 2 dB to 20 dB, in increments of 2 dB, totaling ten levels, was added to the original ultrasonic signals for each defect radius. The new test set with added noise contains a total of 900 images. As shown in Fig. 6, the time-domain signals with added Gaussian white noise and their corresponding two-dimensional time-frequency images are presented, respectively.

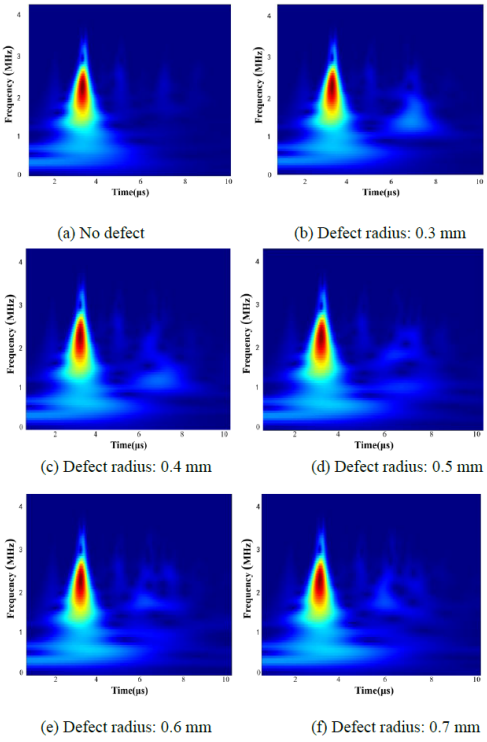

Fig. 5. Two-dimensional time-frequency diagram of defects with different radii

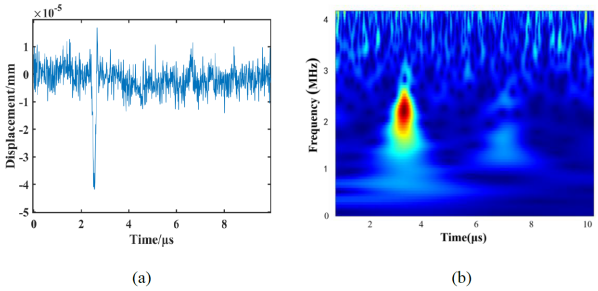

Fig. 6. Noisy images with defect radius of 0.3 mm : (a) time domain signal with SNR of 2dB;(b) Time-frequency images with SNR of 2 dB

2.6. Design of Neural Network Architecture

This paper proposes a convolutional neural network architecture based on the Convolutional Block Attention Module (CBAM-CNN). This network model integrates the CBAM into a CNN, leveraging the feature extraction capabilities of the CBAM module in both channel and spatial dimensions to reduce the impact of redundant information [21]. This enhancement improves the feature extraction and image recognition capabilities of the CNN, thereby further boosting the model's classification performance. The model architecture, as illustrated in Fig. 7, comprises five convolutional layers with a kernel size of 3 × 3, each followed by a max-pooling layer. The CBAM module is embedded after the last convolutional layer. The data from the convolutional and pooling layers are flattened through a flatten layer and then fed into fully connected layers. Three fully connected layers are employed to progressively reduce dimensionality, with a Dropout layer incorporated to set a dropout rate of 0.5 to prevent overfitting. Finally, the

classification results are output through a Softmax layer.

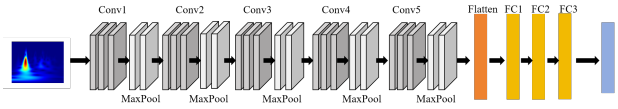

Fig. 7. CBAM-CNN network structure diagram

3. Results and discussion

The experimental environment in this study is a computer running the Windows 10 operating system, equipped with an Intel i5-12400f CPU and an NVIDIA GeForce GTX 1080 graphics card with 8 GB of video memory. The network construction was implemented using Python 3.9, torch 1.12, and CUDA 11.3 on Jupyter Notebook. During the training process, the Adam optimizer was employed, with the learning rate set to 0.0001 and the batch size configured to 32. The training was conducted over 30 epochs. To ensure the accuracy of the results, the experiment was repeated five times, and the average value was taken.

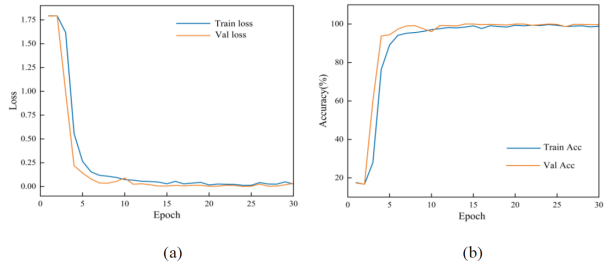

Fig. 8. CBAM-CNN model loss and accuracy graph

Firstly, the model was trained using the time-frequency images converted from the collected raw signals. The test accuracy obtained from five training sessions are 98.32%, 98.65%, 100%, 99.33% and 98.99%, with an average accuracy of 99.06% achieved on the test set. The loss and accuracy curves during the model training process are illustrated in Fig. 8. It can be observed that the training process begins to stabilize after approximately 10 iterations, indicating a relatively fast convergence rate of the model. The CNN model without the attention module, the CAM-CNN model with only the channel attention module, the SAM-CNN model with only the spatial attention module, and the CBAM-CNN model were compared. Their respective average accuracies are shown in Table 2.The results demonstrate that in the weld defect classification task, the CAM-CNN and SAM-CNN models achieved accuracy improvements of 3.49% and 2.12%, respectively, compared to the CNN model. This validates the effectiveness of channel attention mechanisms and spatial attention module in enhancing feature extraction. The proposed CBAM-CNN method achieves a 4.73% accuracy improvement through synergistic integration of dual attention mechanisms, outperforming models with individual attention modules.

To validate the experimental results, the model was subjected to confusion matrix visualization and t-SNE visualization. This article classifies six types of labels based on different sizes of pore defects. Label $0, 1, 2, 3, 4$ correspond to pore radii of 0.3 mm, 0.4 mm, 0.5 mm, 0.6 mm and 0.7 mm respectively, and label 5 represents the no-defect state.These labels are assigned during the data preprocessing stage and the classification probabilities are output through the Softmax layer.The confusion matrix of the model, as shown in Fig. 9 (a), displays the predicted labels on the horizontal axis and the true labels on the vertical axis. It is evident that the model correctly classified all pore defects of varying radii. The t -SNE visualization of the model, depicted in Fig. 9 (c), reveals that the six defect categories are completely separated and independent from each other, demonstrating effective classification performance.

To further investigate the generalization capability of the network model, the ten different types of noisy signals mentioned in Section 2.2, comprising a total of 900 images, were used as a new test set to evaluate the CBAM-CNN model trained on the original signals. The average accuracy from five experiments was taken as the result. The accuracy of the model training are 87.89%, 92.33%, 89.89%, 85.44% and 90.33%, with an average accuracy of 89.18%. The confusion matrix of the model, as shown in Fig. 9 (b), indicates that the model maintains a high defect classification accuracy even under noisy conditions. The t -SNE visualization of the model, depicted in Fig. 9 (d), demonstrates that the features of the defects remain well-separated under noisy conditions, with features of the same defect category being relatively clustered. It is evident that the network model exhibits robust defect classification performance even with varying levels of noise, highlighting its strong robustness and generalization capability.

4. Conclusions

This paper proposes a weld defect detection method based on the integration of laser ultrasonics and CBAM-CNN, aiming to enhance the accuracy and efficiency of weld defect detection through the combination of non-contact non-destructive testing technology and neural networks. Building upon the traditional convolutional neural network, the CBAM is incorporated to strengthen image feature extraction through the channel attention module and spatial attention module, thereby improving the model's

Table 2. Network model comparison

Model	Average accuracy(%)
CNN	94.33
CAM-CNN	97.82
SAM-CNN	96.45
CBAM-CNN	99.06

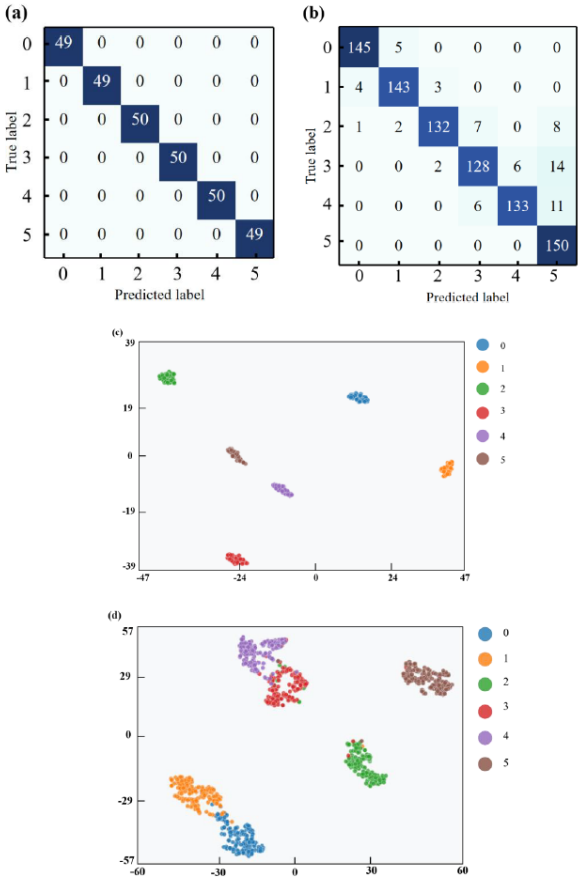

Fig. 9. Confusion matrix of (a) original signal (b) noise signal and t-SNE visualization of (c) original signal (d) noise signal

performance. A numerical simulation model of the interaction between laser ultrasonics and different weld defects is established to obtain the required time-domain ultrasonic signals, which are then transformed into two-dimensional time-frequency images via CWT. Experimental results demonstrate that the model achieves an average accuracy of 99.06% on the test set and 89.18% on the noisy test set, effectively extracting and identifying the characteristics of weld defects for classification. The proposed method, which combines laser ultrasonics with CBAM-CNN, exhibits outstanding performance in detection accuracy and noise resistance, holding significant practical application value and broad development prospects.

5. Acknowledgements

This work was supported by the National Natural Science Foundation of China under Grant No. 62271235 and the Foundation of State Key Laboratory of Dynamic Testing Technology under Grant No. 2022-SYSJJ-10.

References

[1] W. Zeng, M. Cai, P. Wang, T. Lu, and F. Yao, (2020) *"Application of laser ultrasonic technique for detecting weld defect based on FDST method"* **Optik *221***: 165366. DOI: 10.1016/j.ijleo.2020.165366.

[2] W. J. Shao, Y. Huang, and Y. Zhang, (2018) *"A novel weld seam detection method for space weld seam of narrow butt joint in laser welding"* **Optics & Laser Technology *99***: 39–51. DOI: 10.1016/j.optlastec.2017.09.

[3] Y. Lu, Z. Zhu, A. Yin, X. Xu, Z. Zhang, and X. Shu, (2023) *"Evaluation of corrosion resistance of 316L stainless steel by laser ultrasonic nondestructive testing technology"* **Materials Research Express *10***(9): 096519. DOI: 10.1088/2053-1591/acf6ae.

[4] X. Kou, C. Pei, T. Liu, S. Wu, T. Liu, and Z. Chen, (2021) *"Noncontact testing and imaging of internal defects with a new Laser-ultrasonic SAFT method"* **Applied Acoustics *178***: 107956. DOI: 10.1016/j.apacoust.2021.107956.

[5] G. Davis, R. Nagarajah, S. Palanisamy, R. A. R. Rashid, P. Rajagopal, and K. Balasubramaniam, (2019) *"Laser ultrasonic inspection of additive manufactured components"* **The International Journal of Advanced Manufacturing Technology *102***(5): 2571–2579. DOI: 10.1007/s00170-018-3046-y.

[6] N. Okuyama, K. Nomura, T. Sano, K. Kadota, S. Nitta, T. Era, and S. Asai, (2023) *"Study on Detecting Method of Internal Defects by Laser Ultrasonics in Lap Joint Welding of Galvanized Steel Sheet and Finite Element Analysis of Its Detectability"* **Applied Sciences *13***(20): 11515. DOI: 10.3390/app132011515.

[7] S. Nothdurft, A. Springer, S. Kaierle, H. Ohrdes, J. Twiefel, J. Wallaschek, M. Mildebrath, H. J. Maier, T. Hassel, and L. Overmeyer, (2018) *"Laser welding of dissimilar low-alloyed steel-steel butt joints and the effects of beam position and ultrasound excitation on the microstructure"* **Journal of Laser Applications *30***(3): DOI: 10.2351/1.5040607.

[8] L. Ding, Q. Lu, S. Liu, R. Xu, X. Yan, X. Xu, M. Lu, and Y. Chen, (2022) *"Quality inspection of micro solder joints in laser spot welding by laser ultrasonic method"* **Ultrasonics *118***: 106567. DOI: 10.1016/j.ultras.2021.106567.

[9] H. Alqahtani and A. Ray, (2024) *"Convolutional neural network for risk assessment in polycrystalline alloy structures via ultrasonic testing"* **Fatigue Fracture of Engineering Materials Structures *47***(1): 140–152. DOI: 10.1111/ffe.14172.

[10] S.-H. Park, J.-Y. Hong, T. Ha, S. Choi, and K.-Y. Jhang, (2021) *"Deep learning-based ultrasonic testing to evaluate the porosity of additively manufactured parts with rough surfaces"* **Metals *11***(2): 290. DOI: 10 . 3390 / met11020290.

[11] N. Munir, H.-J. Kim, J. Park, S.-J. Song, and S.-S. Kang, (2019) *"Convolutional neural network for ultrasonic weldment flaw classification in noisy conditions"* **Ultrasonics *94***: 74–81. DOI: 10.1016/j.ultras.2018.12.001.

[12] J. Zhao, T. Hu, and Q. Zhang, (2022) *"A wavelet packet transform and convolutional neural network method based ultrasonic detection signals recognition of concrete"* **Sensors *22***(10): 3863. DOI: 10.3390/s22103863.

[13] T. ZHU, B. Song, J. Mao, and G. LIAN, (2022) *"PAUT data intelligent analysis method of welding seams based on deep learning"* **Journal of Beijing University of Aeronautics and Astronautics *48***(3): 504–513. DOI: 10.13700/j.bh.1001-5965.2020.0578.

[14] Y. Yan, Y. Chen, P. Jia, et al., (2020) *"Numerical simulation of ultrasonic waves generated by laser in plate"* **Applied Laser *40***(1): 169–175. DOI: 10.14128/j.cnki.al.20204001.169.

[15] Z. Yang, H. Yang, T. Tian, D. Deng, M. Hu, J. Ma, D. Gao, J. Zhang, S. Ma, L. Yang, et al., (2023) *"A review on guided-ultrasonic-wave-based structural health monitoring: From fundamental theory to machine learning techniques"* **Ultrasonics *133***: 107014. DOI: 10.1016/j.ultras.2023.107014.

[16] H. Fu, G. Song, and Y. Wang, (2021) *"Improved YOLOv4 marine target detection combined with CBAM"* **Symmetry *13***(4): 623. DOI: 10.3390/sym13040623.

[17] H. Guo, B. Zheng, and H. Liu, (2017) *"Numerical simulation and experimental research on interaction of micro-defects and laser ultrasonic signal"* **Optics & Laser Technology *96***: 58–64. DOI: 10.1016/j.optlastec.2017.04.004.

[18] W. Zeng, X. Zou, and F. Yao, (2020) *"Finite element simulation of phased array laser-generated surface acoustic wave for identification surface defects"* **Optik *224***: 165733. DOI: 10.1016/j.ijleo.2020.165733.

[19] T. Wang, C. Lu, Y. Sun, M. Yang, C. Liu, and C. Ou, (2021) *"Automatic ECG classification using continuous wavelet transform and convolutional neural network"* **Entropy *23***(1): 119. DOI: 10.3390/e23010119.

[20] R. He, K. Wang, N. Zhao, Y. Liu, Y. Yuan, Q. Li, and H. Zhang, (2018) *"Automatic detection of atrial fibrillation based on continuous wavelet transform and 2D convolutional neural networks"* **Frontiers in physiology *9***: 1206. DOI: 10.3389/fphys.2018.01206.

[21] S. Zhang, Z. Liu, Y. Chen, Y. Jin, and G. Bai, (2023) *"Selective kernel convolution deep residual network based on channel-spatial attention mechanism and feature fusion for mechanical fault diagnosis"* **ISA transactions *133***: 369–383. DOI: 10.1016/j.isatra.2022.06.035.